LETTERS
PUBLISHED ONLINE: 5 JANUARY 2014 | DOI: 10.1038/NPHYS2848
nature physics

Spin–layer locking effects in optical orientation of exciton spin in bilayer WSe_2

Aaron M. Jones[1], Hongyi Yu[2], Jason S. Ross[3], Philip Klement[1,4], Nirmal J. Ghimire[5,6], Jiaqiang Yan[6,7], David G. Mandrus[5,6,7], Wang Yao[2] and Xiaodong Xu[1,3]*

Coupling degrees of freedom of distinct nature plays a critical role in numerous physical phenomena[1–10]. The recent emergence of layered materials[11–13] provides a laboratory for studying the interplay between internal quantum degrees of freedom of electrons[14,15]. Here we report new coupling phenomena connecting real spin with layer pseudospins in bilayer WSe_2. In polarization-resolved photoluminescence measurements, we observe large spin orientation of neutral and charged excitons by both circularly and linearly polarized excitation, with the trion spectrum splitting into a doublet at large vertical electrical field. These observations can be explained as a locking of spin and layer pseudospin in a given valley[15], where the doublet implies an electrically induced spin splitting. The observed distinctive behaviour of the trion doublet under polarized excitation further provides spectroscopic evidence of interlayer and intralayer trion species, a promising step towards optical manipulation in van der Waals heterostructures[16] through interlayer excitons.

Exploring the consequences of the interplay between distinct quantum degrees of freedom has been an active theme in modern physics. A salient example is spin–orbit coupling (SOC), which is essential in renowned condensed matter phenomena such as the spin Hall effect[1,2], topological insulators[3,4] and Majorana fermions[5,6]; in cold atom physics in the search for new condensate structures[7]; and in technological applications such as magnetoelectric coupling in multiferroics[8] as well as optical and electrical control of spins for spintronics[9,10]. All of these phenomena arise from the coupling of the motional degree of freedom of a particle with its real spin.

A pseudospin describes another discrete internal degree of freedom of electrons, and in most systems has an orbital origin and can therefore couple to the real spin by SOC as well. An excellent example is found in monolayer transition-metal dichalcogenides (TMDCs), which have attracted a significant amount of interest recently[12,13,17–21]. The inversion symmetry breaking allows for an effective coupling between the real spin and valley pseudospin[14] (the latter indexes the degenerate extrema of the electron energy dispersion in momentum space). In the presence of mirror and time-reversal symmetry, SOC can be manifested as an out-of-plane spin splitting with a valley-dependent sign (Fig. 1a).

Bilayer two-dimensional materials (for example, bilayer graphene[22–26] and bilayer TMDCs; ref. 15) possess another distinct degree of freedom known as the layer pseudospin. An electronic state localized to the upper or lower layer can be labelled with pseudospin up or down, respectively, which corresponds to electrical polarization. In a layered material with spin–valley coupling and AB stacking, such as bilayer TMDCs, both spin and valley are coupled to layer pseudospin[15]. As shown in Fig. 1a, because the lower layer is a 180° in-plane rotation of the upper layer, the out-of-plane spin splitting has a sign that depends on both valley and layer pseudospins. Interlayer hopping thus has an energy cost equal to twice the SOC strength λ. When 2λ is larger than the hopping amplitude $t_\perp$, a carrier is localized in either the upper or lower layer depending on its valley and spin state. In other words, in a given valley, the spin configuration is locked to the layer index. This is schematically illustrated in Fig. 1b,c. This spin–layer locking permits electrical manipulation of spins through gate control of layer polarization, which may lead to new magnetoelectric effects and quantum logic[15].

Here, we report experimental signatures of coupling between this layer pseudospin and the spin and valley degrees of freedom in bilayers of WSe_2 (bi-WSe_2). In contrast to MoS_2 (ref. 19), the high quality of WSe_2, in addition to much larger SOC, provides an excellent system for observing spin–layer locking. Although bi-WSe_2 is an indirect-bandgap semiconductor, the near degeneracy between indirect and direct transitions permits us to efficiently monitor direct-gap photoluminescence from the K valleys[12,13,27]. Electrons in the conduction bands near the K valleys exhibit a spin splitting $2\lambda \sim 30$–40 meV, which is two orders of magnitude larger than the interlayer hopping amplitude $t_\perp$ at the $\pm$K points (see Supplementary Information 1). For holes, $2\lambda \sim 450$ meV and $2\lambda/t_\perp \sim 7$ (ref. 15). Large 2λ to $t_\perp$ ratios ensure that interlayer hopping for both electrons and holes is suppressed, achieving a spin–layer locking effect.

We first identify the exciton states in bi-WSe_2 through gate-dependent photoluminescence measurements (see Methods)[28,29]. Figure 2a shows the photoluminescence intensity from direct-gap exciton emission as a function of backgate voltage (V_g) and photon energy. By comparing the gate-dependent patterns and emission energies of monolayer (Supplementary Section 2)[29] and bilayer WSe_2, we can identify the weak feature near 1.74 eV and $V_g = 0$ as neutral exciton (X^0) emission, whereas the peak near 1.71 eV at positive or negative V_g corresponds to negative (X^-) or positive (X^+) trions, respectively. The photoluminescence peak near 1.63 eV arises from impurity-bound excitons. Figure 2c shows photoluminescence spectra at three selected values of V_g. The peaks here coincide with the lowest energy absorption feature shown in Fig. 2b, the gate-dependent differential reflectivity obtained by white-light reflection (Supplementary Section 3).

[1]Department of Physics, University of Washington, Seattle, Washington 98195, USA, [2]Department of Physics and Center of Theoretical and Computational Physics, University of Hong Kong, Hong Kong, China, [3]Department of Materials Science and Engineering, University of Washington, Seattle, Washington 98195, USA, [4]Department of Physics, Justus-Liebig-University, Giessen 35392, Germany, [5]Department of Physics and Astronomy, University of Tennessee, Knoxville, Tennessee 37996, USA, [6]Materials Science and Technology Division, Oak Ridge National Laboratory, Oak Ridge, Tennessee 37831, USA, [7]Department of Materials Science and Engineering, University of Tennessee, Knoxville, Tennessee 37996, USA. *e-mail: xuxd@uw.edu

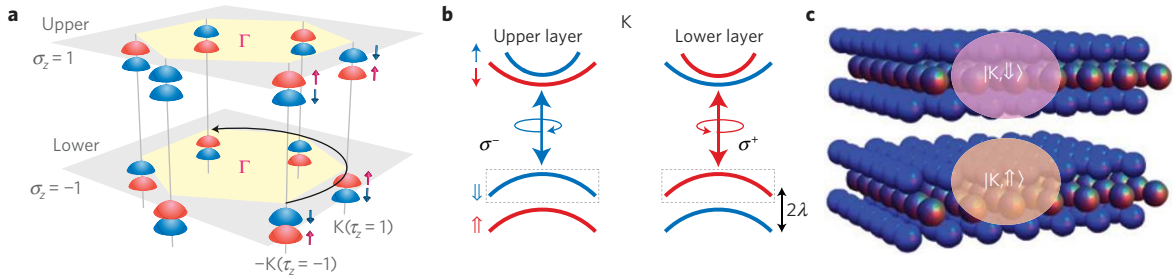

Figure 1 | Coupled spin, valley and layer degrees of freedom in bilayer WSe_2. a, AB stacking order in bilayer TMDCs corresponds to 180° rotation of the lattice between layers, leading to an effective layer pseudospin σ_z. T_z and Γ indicate the valley index and first Brillouin zone centre, respectively. **b**, Cartoon depicting excitation/emission processes in the K valley of bilayer WSe_2. Spin configuration is indicated by ⇑ (↑) for holes (electrons). The same for the −K valley is obtained by time reversal. **c**, Depiction of spin-down (-up) hole states localized in the upper (lower) layer in the K valley.

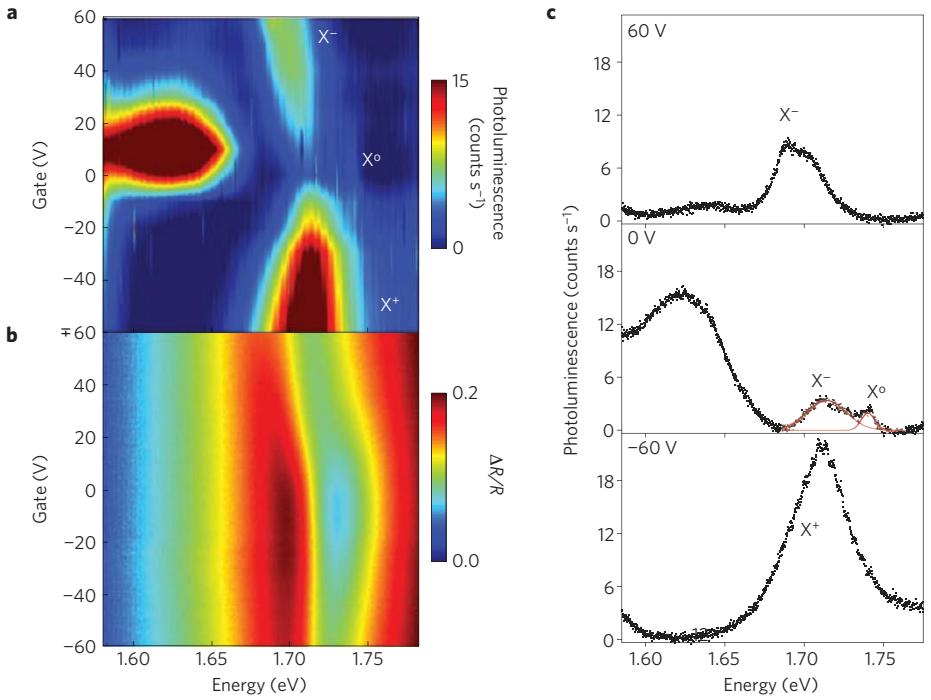

Figure 2 | Photoluminescence and differential reflectivity versus gate. a, Photoluminescence intensity as a function of gate voltage and photon energy with labelled neutral exciton (X^0), and negative (X^-) and positive (X^+) trion emission. **b**, Corresponding differential reflectance showing relationship of X^-/X^+ emission to the absorption feature. **c**, Photoluminescence spectra extracted at +60, 0 and −60 V, showing excitonic peaks X^-, X^0 and X^+, respectively. Red lines in the 0 V spectrum show Lorentzian peak fits.

Next we show that large and electrically tunable exciton spin polarization can be generated in bi-WSe_2 by optical pumping. Figure 3a shows the polarization-resolved photoluminescence under σ^+ excitation for σ^+ (black curve) and σ^- (red curve) detection, at selected V_g. The degree of polarization is large for X^0, X^+ and X^- at all voltages, demonstrating the generation of large exciton spin polarizations. Interestingly, for V_g above 60 V, a doublet structure emerges in the X^- spectrum for σ^+ (co-polarized) detection, with an increasing separation between peaks at higher V_g. We label the peaks I and II as shown in the bottom right of Fig. 3a. Note that the position of peak II coincides with the single peak present for σ^- (cross-polarized) detection. The doublet can be fitted by a dual Lorentzian line shape (blue lines).

We define the degree of circular polarization as $\eta_\sigma = (\mathrm{PL}(\sigma^+) - \mathrm{PL}(\sigma^-))/(\mathrm{PL}(\sigma^+) + \mathrm{PL}(\sigma^-))$, where $\mathrm{PL}(\sigma^\pm)$ is the detected photoluminescence with $\sigma^\pm$ polarization. The extracted η_σ of the trion peak as a function of V_g is shown in Fig. 3b. For V_g below 60 V, the doublet separation is not resolved and η_σ is obtained at the peak position without fitting. The inset shows a zoomed-in view of η_σ centred at 0 V, where an enhancement of an already large η_σ for increasing $|V_g|$ is observed. The doublet emerges for V_g above 60 V with differing degrees of exciton spin orientation for the two peaks. For simplicity, we plot just the σ^+ branch of η_σ, with the black and blue dots indicating the polarization of trion peaks I and II, respectively, obtained from the peak fittings (see Supplementary Section 4 for fitting parameters). Figure 3c shows the peak splitting as a function of V_g under σ^+-polarized excitation (black squares).

The gate-dependent photoluminescence in Fig. 2a shows the crossover between X^+ and X^- near $V_g = 0$, which demonstrates that the sample is nearly intrinsic, without substantial external doping from substrate effects or impurities. The inset in Fig. 3b shows that the polarization minimum is near $V_g = 0$. We also performed second harmonic generation measurements (Supplementary Section 5), which showed more than two orders of magnitude suppression of second harmonic generation in bi-WSe_2 compared with monolayer[30]. These results imply the presence of inversion symmetry in unbiased bi-WSe_2. Therefore, it is not possible that the circularly polarized photoluminescence near $V_g = 0$ stems from

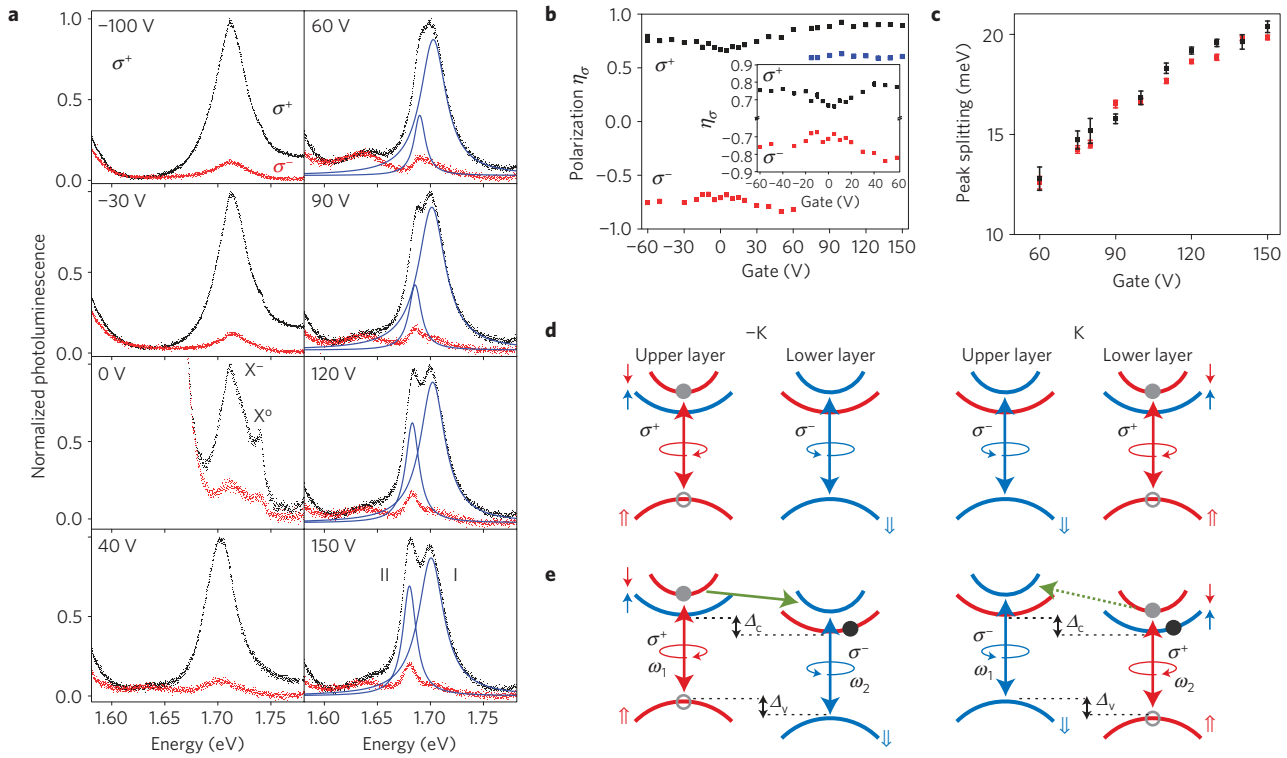

Figure 3 | Optical orientation of spin and gate-induced peak splitting in trions. a, Normalized photoluminescence spectra versus photon energy at selected gate voltages for σ^+-polarized excitation and σ^+ (black curve) and σ^- (red curve) detection. Blue lines in plots for $V_g > 50$ V show Lorentzian peak fits of σ^+ detection data. **b**, Trion photoluminescence circular polarization, η_σ, as a function of gate voltage, where black (red) data indicate σ^+ (σ^-) excitation. For $V_g > 50$ V, the trion peak splits and black (blue) data correspond to η_σ of peak I (II) under σ^+ excitation. Inset: zoom-in showing enhancement of η_σ with applied gate voltage for both σ^+ (black) and σ^- (red) excitation. **c**, Trion peak splitting as a function of applied gate voltage for circularly (black) and linearly (red) polarized excitation. Error bars indicate standard deviation of peak position from fitting. **d**, Schematic depiction of the formation of excitons in both K and −K valleys under σ^+ excitation in unbiased bilayer WSe_2, resulting in no net valley polarization. Hollow (solid) circles denote holes (electrons). Grey circles denote photo-excited electron–hole pairs. **e**, Schematic of electric-field-induced band shifts and electron spin relaxation pathways (green arrows). Emission from the upper and lower layers is at ω_1 and ω_2, respectively, whose splitting originates in the difference between the conduction (Δ_c) and valence (Δ_v) band energy shifts with gate electric field.

valley polarization, as demonstrated in single-layer materials[17–19], which requires explicit inversion symmetry breaking[14]. Rather, it originates from exciton spin polarization, a consequence of the spin optical selection rules present for both inversion-symmetric and asymmetric bilayers with large SOC (ref. 15).

We attribute the large exciton spin polarization, together with the emergence of an X^- doublet at high electric field, to the spin–layer locking effect[15], which leads to an enhanced spin lifetime and electrically induced spin splitting. Figure 3d shows the energy level diagram of AB-stacked bi-WSe_2 without an applied electric field. Single and double arrows denote the spin configurations of electrons and holes, respectively. As there are many possible trion configurations, we show only electron–hole pairs that emit significant photoluminescence. Under σ^+ excitation, the transition involving spin-up hole states is excited in both +K and −K valleys with equal strength and no valley polarization is generated. As a result of the spin–layer locking (Fig. 1b,c), intra-valley spin flips are suppressed as the spin-up and -down states are localized in opposite layers. Accordingly, the spin relaxation time can be long compared with the exciton lifetime, leading to large exciton spin orientation[31].

A perpendicular electric field creates a potential difference between upper and lower layers, which lifts the energy degeneracy between spin-up and -down states localized in opposite layers for a given valley. The result is an electrically induced spin Zeeman splitting. The spin splitting for electrons, Δ_c, is larger by a few per cent than that for holes, Δ_v, owing to the larger $2\lambda/t_\perp$ ratio (Supplementary Section 6). This difference leads to two distinct emission frequencies, that is, a higher frequency ω_1 for electron–hole recombination in the upper layer and a lower emission frequency ω_2 for the lower layer (Fig. 3e). When $\omega_1 - \omega_2$ becomes larger than the spectral linewidth, the trion peak splits into a doublet as shown in Fig. 3a.

With this doublet resolved at large gate values, we observe differing degrees of polarization for the two trion peaks, which further corroborates spin–layer locking. Specifically, the polarization of peak I centred at the higher frequency ω_1 is larger than that of peak II centred at ω_2. As the spectra in Fig. 3a show, for $V_g > 50$ V, the weak photoluminescence feature acquired under σ^+ excitation with σ^- detection (red curves) is always centred at ω_2. Figure 3e depicts the mechanism for the reduced polarization of peak II compared with peak I. Considering σ^+ excitation, σ^+-polarized photoluminescence at ω_1 and ω_2 comes from electron–hole recombination in the upper layer in the −K valley and the lower layer in the +K valley, respectively. Through a spin-flip and dissipation of the energy Δ_c to the environment, the photo-excited electron in the upper layer of the −K valley can relax to the lower layer within the same valley, which leads to σ^- photoluminescence at energy ω_2, corresponding to peak II (Supplementary Fig. 7). In contrast, σ^-PL at energy ω_1 requires absorption of the energy Δ_c to flip the photo-excited electron spin from the lower to the upper layer in the +K valley. Such spin-flip processes are strongly suppressed as $\Delta_c \gg k_B T$ under the applied field necessary to resolve the doublet. Therefore, photoluminescence at ω_1 exhibits larger η_σ than at ω_2.

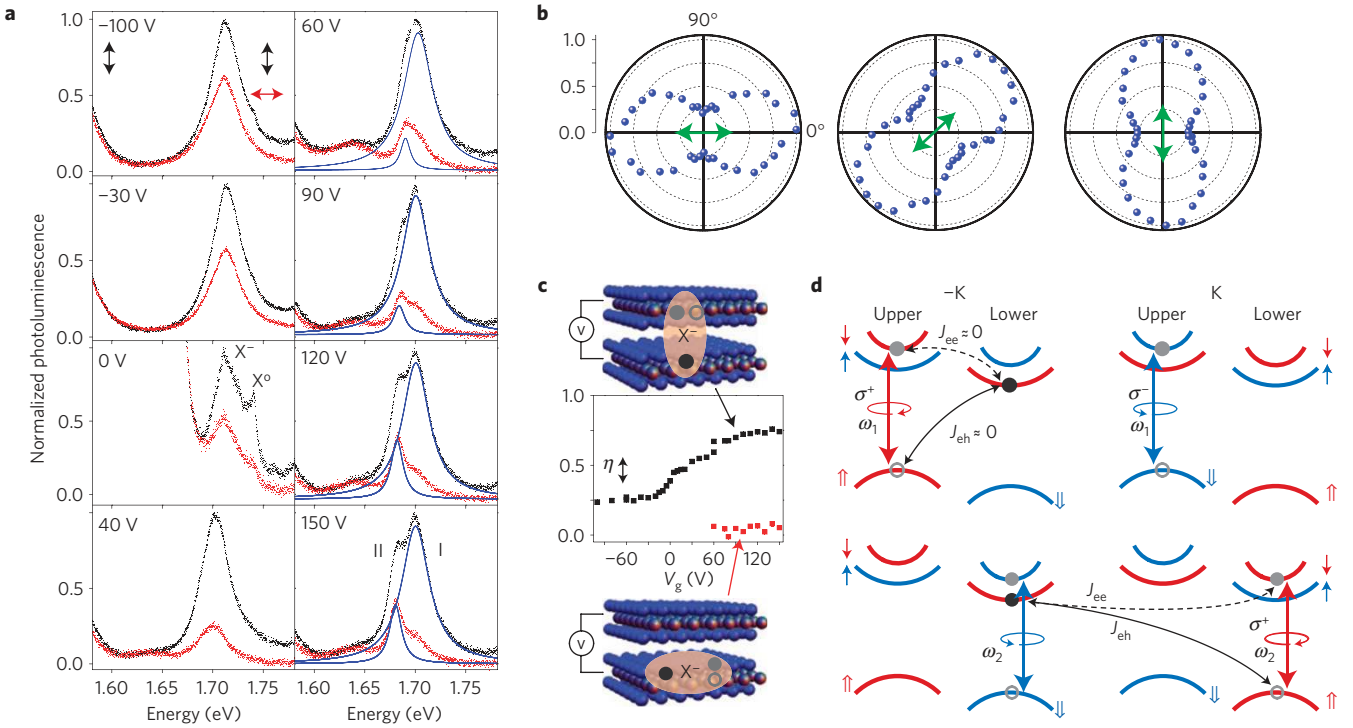

Figure 4 | Linearly polarized excitation of interlayer and intralayer trions. a, Normalized photoluminescence spectra versus photon energy at selected gate voltages for vertically (↕) polarized excitation and vertical (↕, black) and horizontal (↔, red) detection. Blue lines in plots for $V_g > 50$ V show Lorentzian peak fits of data for vertically polarized detection. **b**, Polar plots showing normalized magnitude of trion peak height as a function of detection angle, at $V_g = 0$. Green arrow indicates incident polarization direction. **c**, Trion linear polarization, $\eta_{\updownarrow}$, as a function of gate voltage for vertically polarized excitation (centre), with corresponding depictions of interlayer (top) and intralayer (bottom) trions. For $V_g > 50$ V, the trion peak splits. Black and red data correspond to $\eta_{\updownarrow}$ of peak I (interlayer trions) and peak II (intralayer trions), respectively. **d**, Cartoons depicting a superposition of valley trion configurations giving rise to trion peaks I (top) and II (bottom). Owing to negligible exchange interactions (J_{eh}, J_{ee}), surviving inter-valley coherence for interlayer trion configurations leads to large linear polarization at ω_1 (top), whereas the presence of finite exchange interactions for intralayer configurations eliminates linear polarization at ω_2 (bottom).

In the light of the clear asymmetry of trion peak splitting with applied gate, we note that the energy difference between ω_1 and ω_2 also has a contribution from the different binding energies for each trion configuration. We consider only the lowest energy configurations of optically active trions, where the extra electron or hole is in the lowest energy band (Fig. 3e and Supplementary Fig. 8). For the X^- configuration that emits at ω_1, the electron–hole pair is in the upper layer and the excess electron is in the lower layer (interlayer trion). Conversely, all three particles are localized in the lower layer for X^- at ω_2 (intralayer trion). The larger wavefunction overlap in the latter case leads to larger trion binding energies for peak II than peak I. This effect enhances the X^- energy splitting, that is, $\omega_1 - \omega_2 = (\Delta_c - \Delta_v) + |\delta E_B|$, where δE_B denotes the binding energy difference between interlayer and intralayer trions. Similar analysis for the X^+ trion shows that $\omega_1 - \omega_2 = (\Delta_c - \Delta_v) - |\delta E_B|$ (Supplementary Section 8). From the measured trion binding energy of ~30 meV, we estimate δE_B to be several milli-electron volts. Thus, the binding energy difference may cancel the electric-field-induced splitting and lead to the negligible splitting of X^+ that we observe.

We also examined the degree of linear polarization of the photoluminescence under linearly polarized excitation, which provides clear evidence for the observation of intralayer and interlayer trions, in addition to further revealing the electrically tunable optical orientation of in-plane excitonic spin and confirming the spin–layer locking effect. Figure 4a shows polarization-resolved photoluminescence spectra at selected V_g under vertically polarized excitation and for vertically (↕) and horizontally (↔) polarized detection. In contrast to the observation of linearly polarized photoluminescence for only neutral excitons in monolayer WSe_2 (ref. 29), we observe strong linear polarization for both neutral and charged excitonic states in bi-WSe_2 (see graph for $V_g = 0$, Fig. 4a). Measuring emitted photoluminescence for arbitrary incident polarization angles (green arrows) shows that the trion photoluminescence polarization direction always coincides with that of the incident light (Fig. 4b). This demonstrates insensitivity of the photoluminescence polarization to sample orientation and thus rules out crystal anisotropy as an explanation.

Defining the degree of linear polarization as $\eta_{\updownarrow} = (\mathrm{PL}(\updownarrow) - \mathrm{PL}(\leftrightarrow))/(\mathrm{PL}(\updownarrow) + \mathrm{PL}(\leftrightarrow))$, where $\mathrm{PL}(\updownarrow)$ and $\mathrm{PL}(\leftrightarrow)$ indicate co-linear and perpendicular polarization detection, respectively, we extract the degree of polarization $\eta_{\updownarrow}$ of trions as a function of gate, shown in Fig. 4c. We find that $\eta_{\updownarrow}$ levels out to 0.25 for $V_g < 0$, and increases monotonically for $V_g > 0$. For $V_g > 60$ V, the doublet emerges and the peak splitting matches that obtained under circularly polarized excitation (red squares, Fig. 3c). The polarization is calculated for each doublet peak after fitting. Interestingly, $\eta_{\updownarrow}$ of peak I continues to increase monotonically whereas for peak II it hovers near zero. This can easily be seen by polarization-resolved photoluminescence under vertically polarized excitation at $V_g = 150$ V (Fig. 4a). We obtain the vertically polarized component at ω_2 (blue line) by fitting the data taken with vertically polarized detection (black curve). The extracted vertically polarized photoluminescence at ω_2 matches the measured horizontally polarized component (red dots), indicating negligible linear polarization of peak II. Applying the same procedure at other V_g, we determine that linearly polarized emission comes only from peak I.

As demonstrated in monolayer WSe_2 (ref. 29), isotropic linear polarization can arise from the optical generation of a coherent superposition of excitonic states in the K and −K valleys, which must have identical emission energies and final electronic states on electron–hole recombination. For X^+ in bi-WSe_2, this is allowed only for the interlayer trion configuration (Supplementary Section 9). For X^-, the lower panel of Fig. 4d shows the ground-state configuration for emission at ω_2, which is an intralayer trion with all three particles localized in the same lower layer. As the exchange interaction with the excess electron destroys the inter-valley coherence of the electron–hole pair, no linear polarization is observed at ω_2. Intralayer trion configurations are basically the same as those in monolayer WSe_2, and our observation here is in agreement with the absence of linearly polarized X^- photoluminescence in monolayers[29]. In contrast, for interlayer X^- emission at ω_1 (upper part of Fig. 4d), the excess electron is in the layer opposite the electron–hole pair and the exchange interaction as a dephasing mechanism between σ^+ and σ^- emission is largely suppressed. Our results thus provide spectroscopic means to distinguish intralayer and interlayer excitonic states and demonstrate optical generation of a coherent superposition of distinct valley configurations of interlayer trions.

Methods

WSe_2 bilayers were obtained through mechanical exfoliation[11] of bulk WSe_2 crystals onto 300 nm SiO_2 on a Si substrate. Patterning the bilayers into field-effect transistor geometries was done using an FEI Sirion scanning electron microscope with a Nabity nanometre pattern generation system. Device contacts consisting of 5 nm/50 nm V/Au were evaporated using an electron beam evaporator, followed by standard hot-acetone lift-off techniques. Polarized photoluminescence studies were performed with samples mounted in a low-temperature microphotoluminescence cryostat (Janis). Circularly polarized excitation and photoluminescence readout was accomplished using a Fresnel rhomb prism (CVI), and subsequently analysed with a linear polarizer. All studies were performed at a sample temperature of 30 K with 1.88 eV laser excitation and a 1.5 μm spot size, unless noted otherwise.

Received 2 September 2013; accepted 30 October 2013; published online 5 January 2014

References

1. Kato, Y. K., Myers, R. C., Gossard, A. C. & Awschalom, D. D. Observation of the spin Hall effect in semiconductors. *Science* **306,** 1910–1913 (2004).
2. Wunderlich, J., Kaestner, B., Sinova, J. & Jungwirth, T. Experimental observation of the spin-Hall effect in a two-dimensional spin–orbit coupled semiconductor system. *Phys. Rev. Lett.* **94,** 047204 (2005).
3. Hasan, M. Z. & Kane, C. L. Colloquium: Topological insulators. *Rev. Mod. Phys.* **82,** 3045–3067 (2010).
4. Qi, X-L. & Zhang, S-C. Topological insulators and superconductors. *Rev. Mod. Phys.* **83,** 1057–1110 (2011).
5. Fu, L. & Kane, C. Superconducting proximity effect and Majorana fermions at the surface of a topological insulator. *Phys. Rev. Lett.* **100,** 096407 (2008).
6. Mourik, V. *et al.* Signatures of Majorana fermions in hybrid superconductor–semiconductor nanowire devices. *Science* **336,** 1003–1007 (2012).
7. Lin, Y-J., Jiménez-García, K. & Spielman, I. B. Spin–orbit-coupled Bose–Einstein condensates. *Nature* **471,** 83–86 (2011).
8. Cheong, S-W. & Mostovoy, M. Multiferroics: A magnetic twist for ferroelectricity. *Nature Mater.* **6,** 13–20 (2007).
9. Žutić, I. & Das Sarma, S. Spintronics: Fundamentals and applications. *Rev. Mod. Phys.* **76,** 323–410 (2004).
10. Pesin, D. & MacDonald, A. H. Spintronics and pseudospintronics in graphene and topological insulators. *Nature Mater.* **11,** 409–416 (2012).
11. Novoselov, K. S. *et al.* Two-dimensional atomic crystals. *Proc. Natl Acad. Sci. USA* **102,** 10451–10453 (2005).
12. Mak, K. F., Lee, C., Hone, J., Shan, J. & Heinz, T. F. Atomically thin MoS_2: A new direct-gap semiconductor. *Phys. Rev. Lett.* **105,** 136805 (2010).
13. Splendiani, A. *et al.* Emerging photoluminescence in monolayer MoS_2. *Nano Lett.* **10,** 1271–1275 (2010).
14. Xiao, D., Liu, G-B., Feng, W., Xu, X. & Yao, W. Coupled spin and valley physics in monolayers of MoS_2 and other group-VI dichalcogenides. *Phys. Rev. Lett.* **108,** 196802 (2012).
15. Gong, Z. *et al.* Magnetoelectric effects and valley-controlled spin quantum gates in transition metal dichalcogenide bilayers. *Nature Commun.* **4,** 15 (2013).
16. Geim, A. K. & Grigorieva, I. V. Van der Waals heterostructures. *Nature* **499,** 419–425 (2013).
17. Cao, T. *et al.* Valley-selective circular dichroism of monolayer molybdenum disulphide. *Nature Commun.* **3,** 887 (2012).
18. Mak, K. F., He, K., Shan, J. & Heinz, T. F. Control of valley polarization in monolayer MoS_2 by optical helicity. *Nature Nanotech.* **7,** 494–498 (2012).
19. Zeng, H., Dai, J., Yao, W., Xiao, D. & Cui, X. Valley polarization in MoS_2 monolayers by optical pumping. *Nature Nanotech.* **7,** 490–493 (2012).
20. Li, X., Cao, T., Niu, Q., Shi, J. & Feng, J. Coupling the valley degree of freedom to antiferromagnetic order. *Proc. Natl Acad. Sci. USA* **110,** 3738–3742 (2013).
21. Kormányos, A. *et al.* Monolayer MoS_2: Trigonal warping, the Γ′ valley, and spin–orbit coupling effects. *Phys. Rev. B* **88,** 045416 (2013).
22. Castro, E. *et al.* Biased bilayer graphene: Semiconductor with a gap tunable by the electric field effect. *Phys. Rev. Lett.* **99,** 216802 (2007).
23. Min, H., Borghi, G., Polini, M. & MacDonald, A. Pseudospin magnetism in graphene. *Phys. Rev. B* **77,** 041407 (2008).
24. San-Jose, P., Prada, E., McCann, E. & Schomerus, H. Pseudospin valve in bilayer graphene: Towards graphene-based pseudospintronics. *Phys. Rev. Lett.* **102,** 247204 (2009).
25. Feldman, B. E., Martin, J. & Yacoby, A. Broken-symmetry states and divergent resistance in suspended bilayer graphene. *Nature Phys.* **5,** 889–893 (2009).
26. Maher, P. *et al.* Evidence for a spin phase transition at charge neutrality in bilayer graphene. *Nature Phys.* **9,** 154–158 (2013).
27. Zhao, W. *et al.* Evolution of electronic structure in atomically thin sheets of WS_2 and WSe_2. *ACS Nano* **7,** 791–797 (2013).
28. Ross, J. S. *et al.* Electrical control of neutral and charged excitons in a monolayer semiconductor. *Nature Commun.* **4,** 1474 (2013).
29. Jones, A. M. *et al.* Optical generation of excitonic valley coherence in monolayer WSe2. *Nature Nanotech.* **8,** 634–638 (2013).
30. Zeng, H. *et al.* Optical signature of symmetry variations and spin–valley coupling in atomically thin tungsten dichalcogenides. *Sci. Rep.* **3,** 1608 (2013).
31. Song, Y. & Dery, H. Transport theory of monolayer transition-metal dichalcogenides through symmetry. *Phys. Rev. Lett.* **111,** 026601 (2013).

Acknowledgements

The authors wish to acknowledge G. Liu and X. Wu for helpful information on the bilayer band structure, and D. Cobden for useful comments. This work is mainly supported by US DoE, BES, Division of Materials Sciences and Engineering (DE-SC0008145). A.M.J. is partially supported by a NSF graduate fellowship (DGE-0718124). H.Y. and W.Y. were supported by the Research Grant Council (HKU705513P) of the government of Hong Kong, and the Croucher Foundation under the Croucher Innovation Award. N.J.G., J.Y. and D.G.M. were supported by US DoE, BES, Materials Sciences and Engineering Division. Device fabrication was completed at the University of Washington Microfabrication Facility and NSF-funded Nanotech User Facility. Second harmonic generation is done at Garvey Imaging Core of the Institute for Stem Cell and Regenerative Medicine.

Author contributions

X.X. and W.Y. conceived the experiments. A.M.J. performed the measurements. J.S.R. fabricated the devices, assisted by A.M.J. and P.K. H.Y., W.Y., A.M.J. and X.X. analysed the results. The WSe_2 crystals were synthesized by N.J.G., J.Y. and D.G.M., who also performed characterization measurements of bulk crystals. A.M.J., X.X., H.Y. and W.Y. co-wrote the paper. All authors discussed the results and commented on the manuscript.

Additional information

Supplementary information is available in the online version of the paper. Reprints and permissions information is available online at www.nature.com/reprints. Correspondence and requests for materials should be addressed to X.X.

Competing financial interests

The authors declare no competing financial interests.